BULLETIN OF THE POLISH ACADEMY OF SCIENCES
TECHNICAL SCIENCES
DOI: 10.24425/bpasts.2024.151383

Optimized Design of Downhole Heater Seal for Oil Shale In-Situ Heat Injection

Qiang Li[1, 2, 3] Qingfeng Bu[3, **] Xiaole Li[3] Hao Zeng[4, *]

[1] State Key Laboratory of Shale Oil and Gas Enrichment Mechanisms and Effective Development, Beijing 100083, China
[2] State Center Research and Development of Oil Shale Exploitation, Beijing 102206, China
[3] College of Construction Engineering, Jilin University, Changchun 130026, China
[4] Sinopec Petroleum Exploration & Production Research Institute, Beijing 100083, China

Abstract. Sealing is an important prerequisite for downhole heater work. This paper proposes a combination of soft and hard and welding sealing programs, which were analyzed using theoretical calculations, numerical simulation, and in-situ testing. The results show that 316 stainless steel can meet the stuffing seal requirements; The first stuffing compresses and gradually reduces, while the second stuffing essentially does not deform. Stuffing deformation to fill the gap in the sealing hole, resulting in a sealing layer. The compression rate is 0.43%, 8.45%, and 12.64%, indicating that the locking stress should be more than 2000 N; The temperature at the weld is heated by heat conduction and distributed in a concentric circle. Thermal stress will influence the 50mm barrier, but the 100mm boundary will be mostly unaffected. Actually, the thermal stress that destroys the weld seal may be reduced by adjusting the heater's output or raising the gas injection rate. During the beginning of the in-situ heat injection, the temperature of the heating rods rises simultaneously with the outlet temperature. As consequently, the two show opposite tendencies. The heat generated by the heating rods will cause the injected gas to be preheated in advance.

Key words: Oil shale; In-situ conversion; Downhole heater; Numerical simulation; High-temperature seal

1. INTRODUCTION

China energy structure is defined as "rich in coal, poor in oil, and low in gas" [1, 2]. As an unconventional energy source, the effective development of oil shale can significantly reduce China reliance on oil and gas, as well as increase China autonomy in the global energy market [3]. In-situ conversion is a sophisticated technology for cracking oil shale subsurface [4, 5], however, the traditional surface heat injection method results in significant heat loss along the heat injection pipeline. Downhole heaters have become the subject of research efforts to increase energy conversion efficiency [6].

Downhole heaters are classified as combustion heaters or electric heaters based on how they generate heat [7-9]. Combustion heaters have substantially lower downhole control stability than electric heaters, hence, electric heaters are more commonly utilized in the in-situ conversion process [10]. However, using bare electrodes for downhole heating still has disadvantages, such as a small heat transfer surface, a poorer thermal conductivity efficiency of the reservoirs, and a longer heating period. As a result, employing electric heating rods as a heating source and improving the heat transfer process of the fluid in the shell process via the folding plate structure to heat the fluid to the ideal condition has become the primary development direction of the heater design [11, 12].

Elastic vibrations during operation, harsh well conditions, high-temperature water vapor, oil and gas, and chemically corrosive gases generated during in-situ mining can all have a negative effect on heaters, regardless of the type of baffle plate construction.

According to previous studies [13-15], the primary cause affecting heater operation is frequently not the destruction of the heater body due to high temperatures, but rather the destruction of the electric heater power supply line, resulting in short circuiting of the electric heater [16]. Furthermore, because the electric heater is located inside the well, in the event of a failure, it can only be maintained at the surface, and the frequent up and down work will have a significant impact on in-situ oil shale extraction. As a result, it is critical that the heater is well sealed [17, 18].

Many conventional sealing materials have failed in high-temperature and high-pressure working environments, leaving only metal and special high-temperature-resistant materials to maintain stable performance [19, 20], with hard metal serving as the main body of the sealing structure [21], which includes screw locking ring seal [22], metal flat cushion seal [23], and diaphragm seal [24]. Screw locking rings are a type of hard connection sealing structure that consists of internal and external sealing. The inner bolt and split ring are tightened, and the preload is transmitted through the tube plate to the inner sealing gasket, resulting in an isolated sealing space; Metal flat cushion seals are forced sealing, the washer and copper gasket are fitted in the sealing groove, tighten the lock nut, and under the preload force given by it, touch and fit with the steel seat; Diaphragm seal, tighten the main bolt to push

the gland, which will withstand the pressure of the tube bundle and serve its job. When pressure fluctuations and thermal expansion cause a tiny amount of distortion, the seal structure has enough elasticity to absorb such fluctuations or deformation, guaranteeing that the seal is unaffected [25].

Although the above sealing method is somewhat stable under vibration, when there is a high gas pressure inside the seal, the metal produces a thermal expansion phenomenon, and the heater sealing is still not assured [26, 27]. compared to the hard seal, the sealing method can also be utilized for flexible sealing [28]; the most common sealing methods are the stuffing seal and the soft metal seal [29, 30]. Stuffing, also known as packing, to fill the packing box filled with stuffing, gland on the packing for axial pressure, through the deformation of the stuffing and the radial force of the spinning shaft surface to achieve the plane seal; Soft metal seal is in the two rigid bodies before sandwiched into the elasticity and rigidity of non-metallic materials, and in the sealing groove face open V-shaped sealing groove, in the V-type groove filled with compression properties of the soft metal, when the nut to apply the preload, the stuffing to produce radial expansion, and the wall surface close fit. Both can maintain good sealing under certain conditions, but the former offers greater thermal stability and broader application possibilities [31].

Jilin University created two pilot projects, Nong'an and Fuyu [32], and conducted oil shale cracking tests at various depths, all of which were successful. Combining the engineering experience of the two in-situ locations [33-35], this group is prepared to conduct in-situ cracking tests using the near-critical water method [36] and a downhole heater as the core equipment. The process employs near-critical water as a mass transfer and extraction agent [37-39], causing a sequence of physical and chemical effects on the organic matter in the oil shale and producing hydrocarbons that are carried out of the bottom of the well by the cycling critical water. The most difficult aspect of designing and fabricating an in-situ heater is sealing it totally. Considering the heater gas pressure fluctuation, vibration resistance, high-temperature resistance, and the need for easy well maintenance and replacement, this paper proposes for the first time a combination of soft and hard sealing between the wiring warehouse and the external cable, as well as welded sealing between the wiring warehouse and the heating warehouse, as the sealing scheme for this test. To verify the rationality and applicability of the sealing scheme, this paper takes the heater sealing structure and its sealing method as the research object, analyzes the sealing effect through theoretical calculations, numerical simulations, and in-situ experiments, and explores the stress-strain characteristics of the stuffing seals and the high-temperature stability of the welding seals, so as to form the highly efficient downhole sealing scheme, and provide.

2. ENGINEERING BACKGROUND PREPARE

2.1. Heater Structure Design.

The downhole electric heater described in this study is divided into a wiring warehouse and a heating warehouse as a whole, and the main components include a high-voltage cable, a wiring post, an insulating cushion layer, a folding flow plate, and an electric heating rod. Among them, the high-voltage cable is connected to the wiring warehouse through the wiring post to supply power to the electric heating rod on the folding plate. The heating rod runs through both the wiring and heating warehouses, and all three are welded together (Fig.1).

2.2. Material.

The sealing process is heavily influenced by the materials used. In the previous preparation, sealing solutions containing high temperature rubber (F_2O, C_8F_{16}), asbestos, and graphite packing were tried, but none of them met the test requirements. As a result, flexible graphite [40] was chosen as the sealing

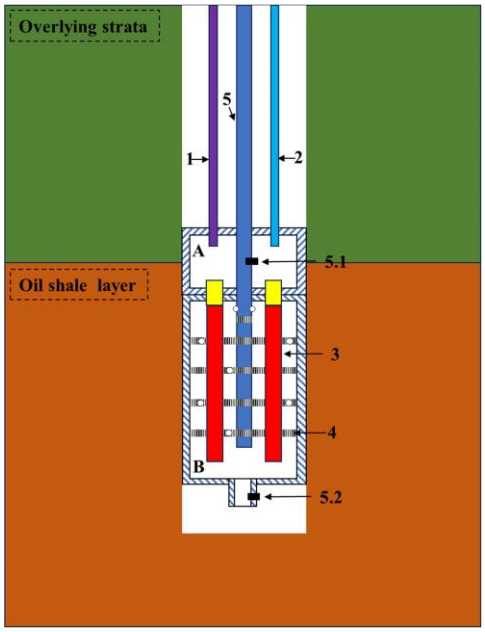

Fig.1. Downhole heater system diagram

Where A is wiring warehouse; B is heating warehouse; 1 is external cable; 2 is sensor lines; 3 is heating rod; 4 is baffle plate; 5 is gas injection pipeline; 5.1 is inlet temperature sensor; 5.2 is outlet temperature sensor

stuffing (as indicated in Table 1), with the following key factors:

- Despite the heat loss of graphite at high temperatures, it can tolerate a maximum temperature of 3650℃;
- Flexible graphite is chemically inert, has a high reaction activation energy, and is almost immune to radiation from chemical media;
- Flexible graphite will adsorb on the surface, forming a thin coating of gas or liquid and providing good sealing performance.

TABLE 1. Flexible graphite parameter

Name	Temperature range (℃)	Density (g/cm^3)	Rebound ratio	Compressibility	Elastic modulus (Gpa)
Flexible graphite	−200～3650℃	0.8~1.8	>15%	>40%	6~15

3. MODEL PARAMETER AND BOUNDARY CONDITION

This study simulates the connection between the wiring warehouse and the external cable, as well as the weld between the heating rod and the heating warehouse, in order to test the sealing efficacy of this sort of sealing solution under downhole operating conditions. The geometric model and dimensions of the stuffing seal structure are presented in Fig.2, while the geometric model and dimensions of the welded seal structure are shown in Fig.3.

The assumptions of the numerical simulation are implemented in this paper:

- The extrusions locking stresses F are, in turn, 1000 N, 2000 N, and 3000 N;
- The fixed restraint is applied at the bottom of the cable and a full constraint is applied at the bottom of the stuffing seal;
- The welded seals are exposed to temperature loads of 400°C, 500°C, and 600°C; the convective heat transfer coefficient is 35.6 W/(m • °C), and a thermal radiation coefficient is 0.3;
- The welding plane is circumferentially constrained and the boundaries of the heating rod are unconstrained.

The Ansys software Mesh is used for meshing, and the model structure is governed by mapping mesh. The three-dimensional model is created using mapping mesh division, and the stuffing sealing structure makes use of a hybrid mesh that consists of tetrahedral and hexahedral meshes. Tetrahedral mesh is used for the lock nut mesh and hexahedral mesh is used for the flexible graphite stuffing portion of the mesh to better replicate the sealing structure. The grid size is 1.5 mm, the number of grid cells is 2×10^4, and the grid nodes are 8.9×10^4; The same grid delineation is used for the welded seal, with the grid size of 2 mm, the number of grid cells is 2.6×10^4, and the grid nodes are 1.21×10^5 (Fig.4 and Fig.5).

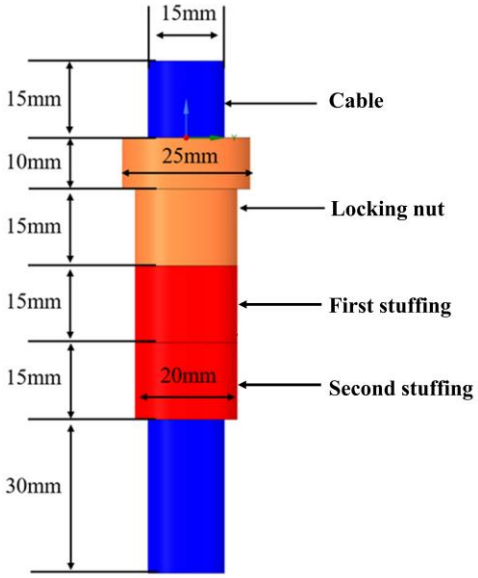

Fig.2. Stuffing seal geometry

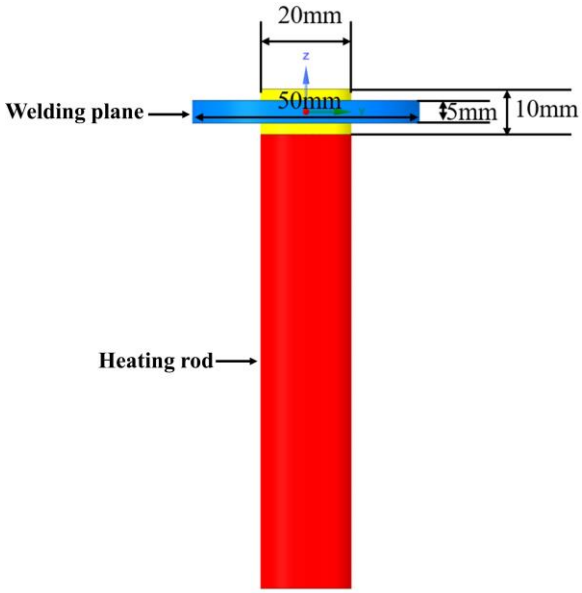

Fig.3. Welded seal geometry

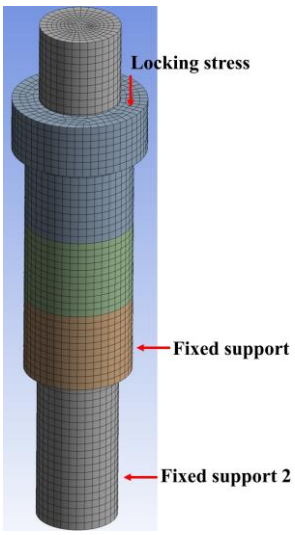

Fig.4. Stuffing seal structural boundary condition

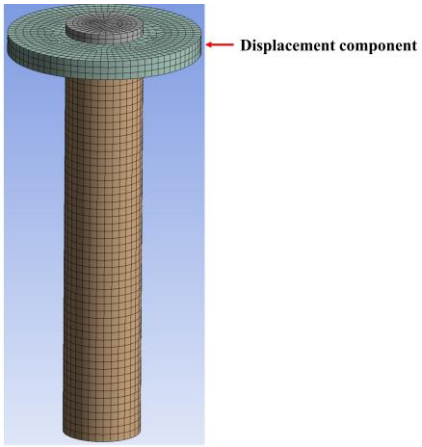

Fig.5. Stuffing seal structural boundary condition

4. RESULTS AND ANALYSIS

4.1. Mechanical Performance Analysis of Sealing Structure.

The stuffing seal structure greatly depends on the lock nut ability to meet locking criteria because it serves as the primary structure for applying locking stress. The locking nut transfers the axial tension F_a to the sealing stuffing, which in turn causes radial strain. As a result, the side wall of the sealing stuffing experiences the following radial stress:

$$\sigma_r(x) = K\sigma_a(x). \quad (1)$$

For the stuffing axial direction, the balance equation is:

$$\frac{\pi}{4}\left({D_0}^2 - {D_i}^2\right)\sigma_a(x) - \frac{\pi}{4}\left({D_0}^2 - {D_i}^2\right) \times \left(\sigma_a(x) + d\sigma_a(x)\right) = df_0 + df_i. \quad (2)$$

$$df_0 = \pi D_0 \mu_0 \sigma_r(x) dx. \quad (3)$$

$$df_i = \pi D_i \mu_i \sigma_r(x) dx. \quad (4)$$

$$\frac{{D_0}^2 - {D_i}^2}{4}\pi = S. \quad (5)$$

Where K is pressure parameter; $\sigma_r(x)$ is radial stress of stuffing box sidewall; $\sigma_a(x)$ is axial stress of stuffing; D_0 is diameter of stuffing box outer wall; D_i is diameter of stuffing box inner wall; df_0 is friction force between stuffing and stuffing box outer wall; df_i is friction force between stuffing and stuffing box inner wall; μ_0 is friction coefficient between stuffing and stuffing box outer wall; μ_i is friction coefficient between stuffing and stuffing box inner wall. For flexible graphite stuffing $\mu_0 = \mu_i = \mu$; S is stuffing cross-sectional area.

Equation (3) can be substituted with the preceding equation to obtain:

$$\frac{d\sigma_a(x)}{\sigma_a(x)} = -\frac{4\mu K}{D_0 - D_i} dx. \quad (6)$$

Equation (6) and the integral for $x = H$:

$$\int_{\sigma_a(x)}^{\frac{P_S}{K}} \frac{d\sigma_a(x)}{\sigma_a(x)} = \frac{2\mu K}{S}\int_x^H dx. \quad (7)$$

$$\sigma_a(x) = \frac{1}{K}P_S e^{\frac{2\mu K}{S}(H-x)}. \quad (8)$$

The compression section axial compression stress at $x = 0$ is:

$$\sigma_a = \frac{1}{K}P_S e^{\frac{2\mu KH}{S}}. \quad (9)$$

To finish the seal, the locking force needed is:

$$F_a = \frac{\pi}{4}(D_0^2 - D_i^2)P_S e^{\frac{2\mu KH}{S}}. \quad (10)$$

When the condition is preloaded, the necessary locking force is:

$$F_1 = \frac{\pi}{4}(D_0^2 - D_i^2)y. \quad (11)$$

The maximum value is considered to be the locking force:

$$F = max\,(F_a, F_1). \quad (12)$$

$$d = \sqrt{\frac{4F}{\pi[\sigma]^t}}. \quad (13)$$

$$\sigma = \frac{F}{0.25\pi(d^2 - d_i^2)}. \quad (14)$$

Where: P_s is shell internal pressure; y is sealing stuffing minimum compression ratio pressure; d is minimum thread diameter which μ =0.18, K =0.28, y =3.5MPa. Taking into account the stuffing radial expansion, D_0 is 8mm, D_i is 20mm, H is 80mm, P_S is 10MPa.

According to equations (1-14), the calculation is F_a=2767 N, F_1=923.16 N, and F =2767 N, d=5.21 mm is the minimum thread diameter required to meet design specifications. Tensile stress at the bottom of the thread is σ=553.4 MPa< $[\sigma]^t$ and the nominal diameter is 6mm, pitch p is 1mm, d is 5.530mm, and d_i is 4.917, as per the GB/T196-2003 standard. Based on theoretical calculations, it is possible to meet the stuffing sealing method strength requirements by employing 316 stainless steel as the production material for the lock nut. In addition, 316 stainless steel is easier to purchase, easier to operate, and more readily replace than other materials. It can withstand greater temperatures, which is necessary to fully fulfill the high temperature working requirements of the heater.

4.2. Stuffing Seal Effect Analysis.

In practical applications, the locking stress is higher than the stress needed for completed sealing, so in this study, locking pressures of 1000, 2000, and 3000 N were applied to the locking nut in order to more accurately assess the stability of the stuffing seal. This is because the locking stress is greater than the stress needed to complete the sealing.

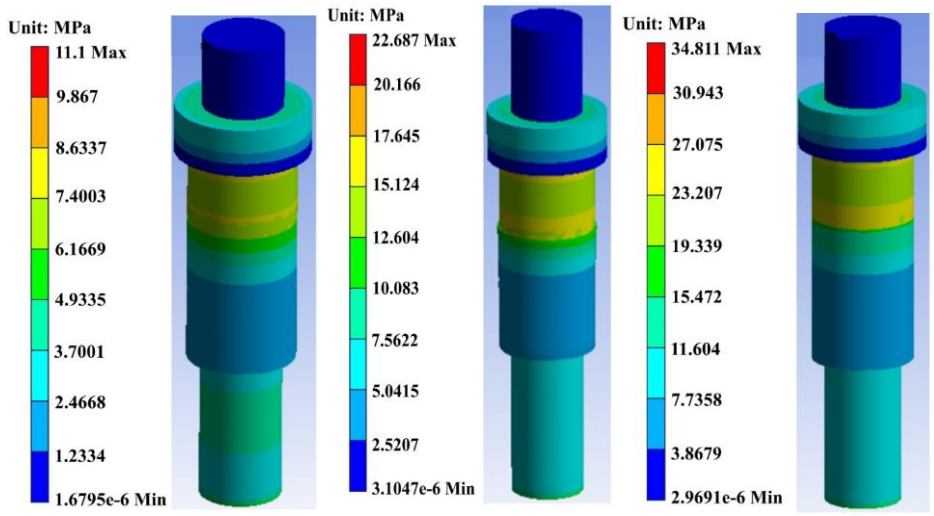

Fig.6. Stuffing seal overall stress diagram，(a) 1000 N; (b) 2000 N; (c) 3000 N

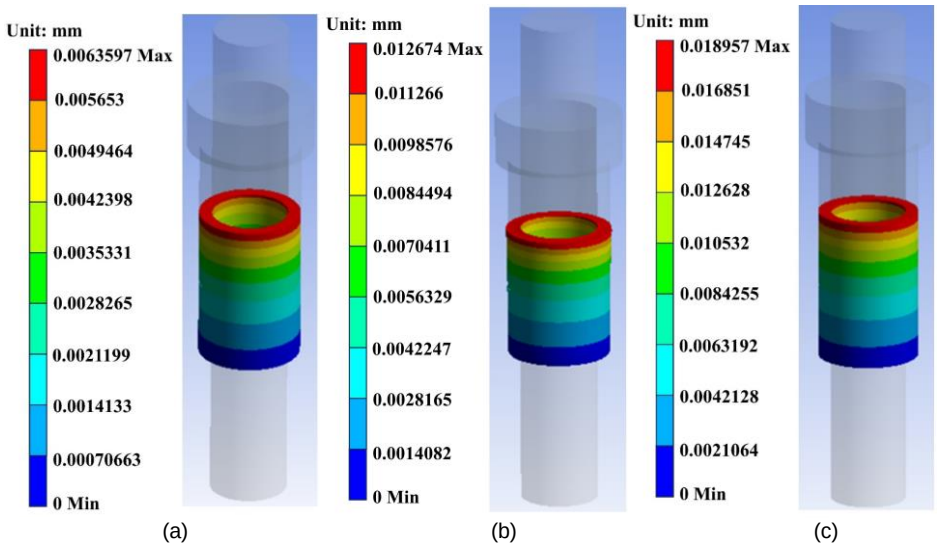

Fig.7. Stuffing overall deformation diagram，(a) 1000 N; (b) 2000 N; (c) 3000 N

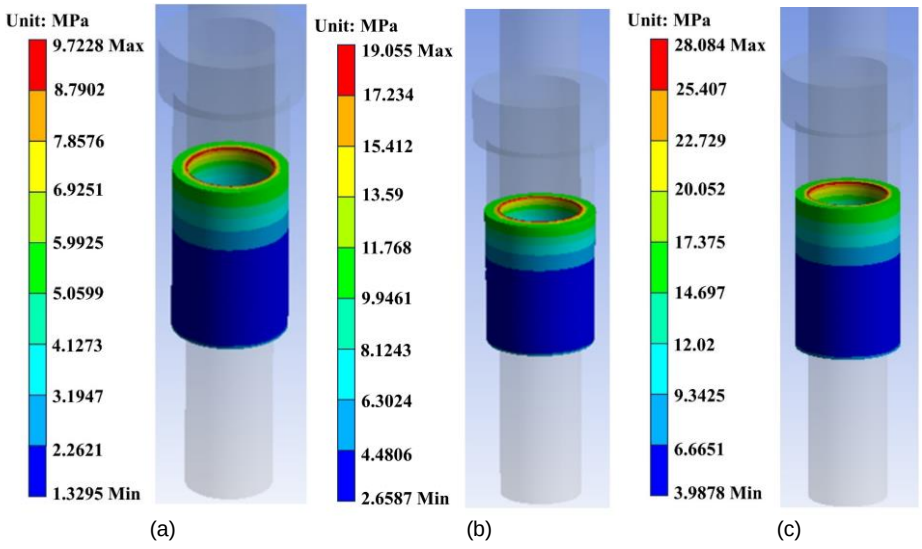

Fig.8. Stuffing force diagram，(a) 1000 N; (b) 2000 N; (c) 3000 N

Fig. 6 illustrates how the locking nut can evenly apply locking stress to the sealing stuffing. This guarantees that, during compression, the sealing stuffing experiences uniform and consistent stress and deformation, a crucial requirement for the stuffing seal to be completed. Due in large part to the lower nut smaller stress area than its upper end, the locking nut stress maximum is mostly focused at its bottom. Using Fig. 7(a) as an example, the locking stress causes a significant amount of compressive deformation in the stuffing. This deformation progressively decreases along the Z-axis, primarily as a result of the stuffing deformation, which attenuates the locking stress. Furthermore, it is evident by comparing the locking stress of the two stuffing that the second stuffing is essentially unaffected. The fundamental cause of this trend of change is the approximate division of the stuffing deformation process into two stages. First, as can be seen in the axial compression deformation of the flexible graphite stuffing, the gas within the internal pores of the stuffing is released, further compressing the distance between the carbon molecules; Second, the stuffing axial compression will cause a radial expansion deformation to fill the gaps between the stuffing and the sealing holes, cables, and locking nuts because of the numerous limitations imposed by the internal cables, sealing holes, and locking nuts. Furthermore, as illustrated in Fig. 8, flexible graphite exhibits some degree of self-lubricating qualities and is better filled with stuffing to form a sealing layer between the lock nut and flexible graphite stuffing contact plane, as well as in the sealing hole wall and the space between the internal cable.

As can be seen in Figs. 7(a), Figs. 7(b) and Figs. 7(c), the first stuffing and the locking nut were where stuffing deformed the most. As the locking stress increased, the compression increased linearly, increasing by 6.3597×10^{-3}, 1.2674×10^{-2}, and 1.8957×10^{-2} mm, respectively. It is clear from the compression rates of the stuffing under various stresses of 0.43 %, 8.45 %, and 12.64 % that a locking stress of 1000 N is insufficient to effectively compact the stuffing and may even cause seal failure; as a result, a locking stress of 2000 N or more is recommended in practical applications. The second stuffing is not able to effectively seal the gap in the sealing hole through deformation, as compared with the first stuffing, which essentially does not deform. The maximum deformation is 6.3192×10^{-3} mm, with a compression rate of 0.42 %, which is comparable to the deformation when the locking stress is 1000 N. in order to take into account the practical applicability. In response to the authors, the primary function of the second stuffing is to act as an insurance layer, keeping the stuffing from being squeezed out of the sealing holes from the bottom of the holes during the compaction sealing process of the first stuffing.

The inner side of the stuffing and the internal cable experience an annular, localized high-pressure stress due to the radial expansion of the stuffing, as depicted in Fig. 8. The operation of downhole heat injection may result in elastic fluctuations of the downhole heater. Which can wear down the cable at that place by rubbing the outer sheath against the inner wall of the locking nut. To increase the sealing structure service life, the inner wall of the locking nut should be polished or chamfered when choosing it.

4.3. Welding Seal Effect Analysis.

The high-temperature load produced by the heating rods is the primary factor impacting the sealing, and it is less susceptible to elastic vibration since the connection between the wire warehouse and the heating warehouse is housed inside the heater. Consequently, 400 °C, 500 °C, and 600 °C are chosen as the temperature conditions, and the thermal stress at the welding location is examined. Furthermore, the heater primary heating elements consist of multiple sets of vertical heating rods, and an analysis is conducted on the boundary ranges measuring 50 and 100 mm from the welding location at 600 ℃ temperature settings.

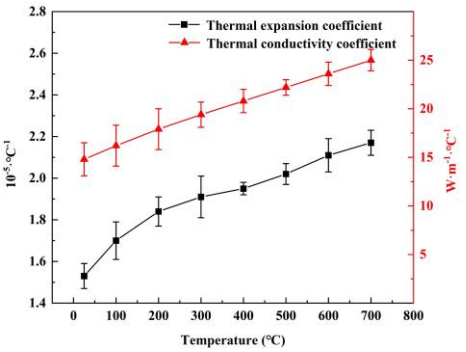

Fig.9. Thermal parameters of the wall surface of the heating rod with temperature curve

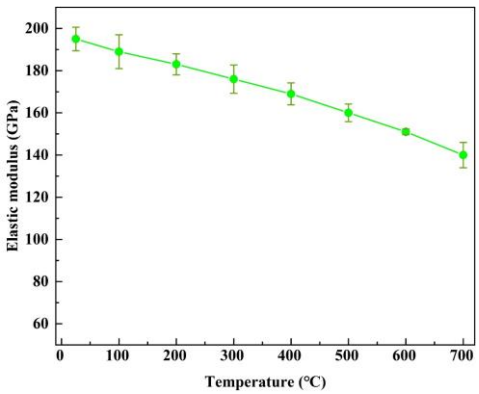

Fig.10. Elastic modulus with temperature cruve

As illustrated in Fig. 9, the heating rod thermal expansion coefficient increases linearly with temperature. This is primarily because the thermal motion of microscopic atoms or molecules is enhanced, increasing the distance between molecules. This, in turn, causes the volume of the heating rod to expand, increasing the coefficient of thermal expansion and potentially causing localized damage at the welding site. As the primary heat carrier, phonons propagation speed increases due to the motion of molecules or microscopic atoms, which also exhibits a similar trend of change in the coefficient of thermal conductivity. This immediately accelerates the rate of heat transfer in the heating rod. The increase in thermal movement of small atoms or molecules brought on by temperature increases is the primary reason of the linear change in both thermal conductivity and coefficient of thermal expansion. As a result, both increase as temperature rises.

In contrast to the other two, the elastic modulus exhibits the opposite trend, as seen in Fig. 10. This is primarily because the thermal motion of microscopic atoms or molecules

intensifies, reducing the interaction force between atoms or molecules. The tendency to produce a greater strain when subjected to the same stress is the macroscopic manifestation of this reduction.

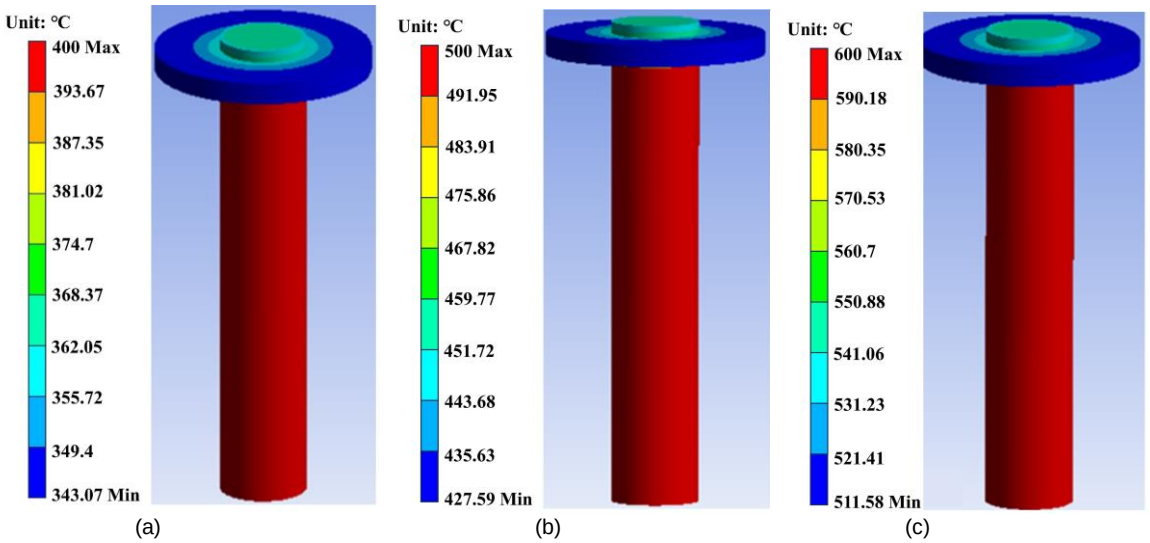

Fig.11. Welding seal temperature field distribution，(a) 400 ℃; (b) 500 ℃; (c) 600 ℃

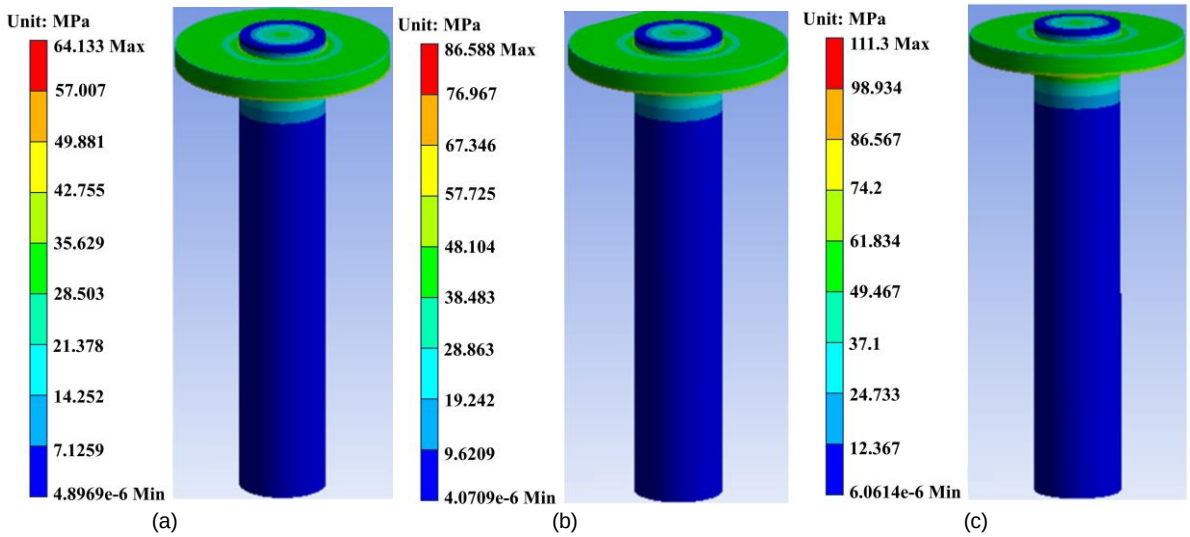

Fig.12. Thermal stress distribution at different temperature conditions，(a) 400 ℃; (b) 500 ℃; (c) 600 ℃

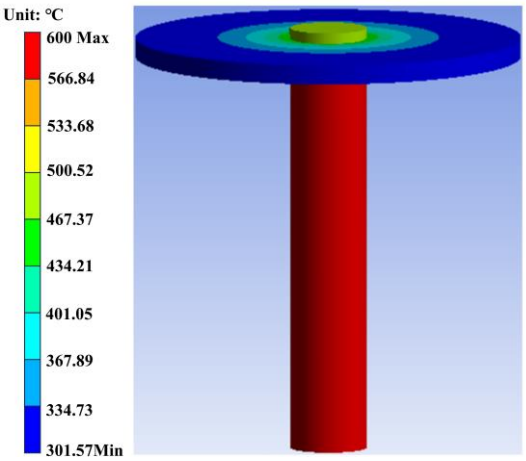

Fig.13. Temperature field distribution at 100mm from the weld

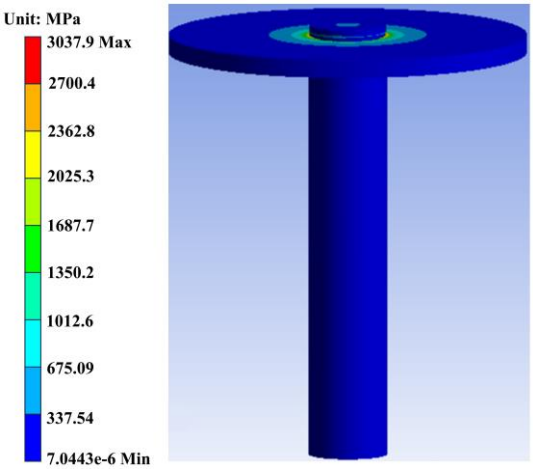

Fig.14. Thermal stress distribution 100mm from the weld

As illustrated in Fig. 11, the primary source of heat is the heating rod beneath the weld. As the temperature of the heat source rises, so does the weld temperature. Heat conduction is the primary method of temperature transfer, which results in the concentric circles that represent the weld temperature distribution. At the welding site, the maximum temperatures recorded were 362.05 °C, 451.72 °C, and 541.06 °C. The temperature loads recorded were 35.629, 48.104, and 61.834 MPa, exhibiting increases of approximately 35.1 % and 28.5 %. The increase linearly between the temperature load and the maximum temperature is in line with the thermal conductivity trend.

Once Fig. 12(c) and Fig. 14 are compared, it can be observed that the weld plane at the boundary 50 mm from the weld is still exposed to significant thermal stresses, while the boundary 100 mm from the weld is almost unaffected. Fourier's law of heat conduction states that the more the conduction distance, the more heat loss occurs along the heat. The temperature difference between the weld and the distance from the 100 mm boundary is approximately 60 % of the weld temperature. Therefore, the authors believe that, given the conditions of this investigation, the heating rod spacing should be maintained above 100 mm in order to prevent heat coupling from affecting the weld seal (Fig. 13). Thermal rupture is most likely to occur there, which would result in the failure of the seal between the wiring warehouse and the heating warehouse. However, with an increase in heating time, thermal stress concentration will still form at the welded seal. Previous research indicates that there is a significant temperature differential between the gas and the heating rod surface when the gas enters the heater. This causes a forced convection phenomenon between the two, meaning that the heat produced on the heating rod surface is removed by the gas flow. As both convective heat transfer time increases with the increase in the flow of the heater, the gas temperature increases, the temperature difference between the both is gradually reduced, the convective heat transfer effect gradually weakened, which means that the same power conditions, the wall of the heater bar there will be a temperature gradient. Therefore, in order to reduce the influence of thermal stress on the weld seal, the heater should be properly adjusted to avoid extended running of the heater at rated power during application. In addition, when the heater seems to run at rated power for a long period when the experiment necessitates it, the flow rate of the injected gas should be raised.

4.4. In-Situ Experiment.

Based on the numerical simulation results shown above, a series of optimizations were made to the heater seal construction to improve its actual applicability, as illustrated in Fig. 15. The Fuyu oil shale in-situ conversion project base was selected to conduct the heater downhole test [41], and before to the test, the ground engineering construction was finished. Afterwards, as illustrated in Fig. 16, the heater was connected, mounted, and dropped into the test well. Procedure for evaluating the downhole heater sealing structure effectiveness:

- After the heater, packer, and tubing are sequentially lowered into the heat injection well, the borehole is sealed.
- The test pressure was 15 MPa, the test temperatures were 400°C, 500 °C, and 600 °C, the heating time was 3 days, 1 day, and 1 day, and the injected gas flow rate was 150 m^3/h.

Fig.15. The electric heater prototype completed

Fig.16. Heater downhole procedure

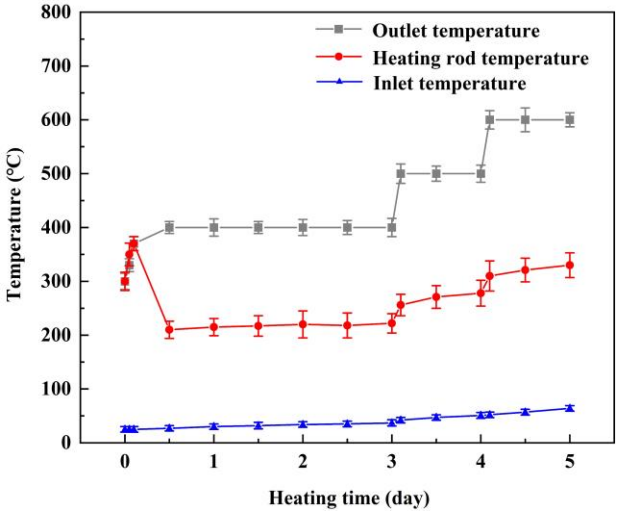

Fig.17. Heater test working parameter

The heater starts on, as shown in Fig. 17, and both the outlet temperature and the heating rod temperature climb quickly to 400 °C. The heating rod temperature and the outlet temperature show the same rising trend during the initial stages of heat injection because the injected gas flow rate is small and cannot completely remove the heat generated by the heating rod. However, as the injection flow rate increases steadily, the gas uses convective heat transfer to carry the heat generated by the

heating rod out, causing the outlet temperature and the heating rod temperature to show the opposite change trend [42]. The heater continues to operate well while the outlet temperature stabilizes at 400 C and the heating rod temperature remains between 210 °C and 220 °C. The surface temperature of the heating rod rises by 20-25 °C for every 100 °C increase in the outlet temperature, indicating that as the heating rod power is raised, the outlet temperature and the heating rod both continue to rise. This indicates that the injected gas cannot fully carry out the heat generated by the heating rod at the current flow rate, which causes the outlet temperature to rise, the temperature differential between the outlet and the heating rod to drop, and the convective heat transfer effect to be weakened. As a result, heat builds up on the surface of the heating rod. The increase in the inlet temperature in the last part of the test could be attributed to the heating of the heater overall, which is the same as the injected gas being pre-heated before it enters the heated bin. This is because the heat buildup on the surface of the heating rod heats both the heater and the gas in the injection well.

This test demonstrates that this kind of sealing can achieve a satisfactory sealing result between the wiring warehouse and the heating rod as well as between the wiring warehouse and the external cable. In the well bottom environment of high temperature and high pressure, the stability of a good sealing effect is still preserved. This paper investigation on the downhole heater sealing structure can yield relevant technical guidelines for the sealing of related downhole heating equipment.

5. CONCLUSIONS

The most important precondition to understanding the heater downhole long-term operation is the research of the sealing effect of the heater sealing structure. Through theoretical calculations, numerical simulations, and field tests, the sealing effect of the sealing structure is examined in this work. The results yielded are as follows:

- Theoretical calculations show that the 316 type stainless steel nut can meet the requirements of the stuffing sealing method, the locking stress is uniformly distributed on the stuffing, the first stuffing experiences a large compression deformation, the deformation is divided into two processes, and the deformation gradually decreases along the Z-axis of the negative direction, while the second stuffing is largely unchanged. The distortion of the stuffing fills the small holes in the sealing hole, forming the sealing layer. Increasing the locking stress leads to a linear rise in compression, with increases of 6.3597×10^{-3}, 1.2674×10^{-2}, and 1.8957×10^{-2} mm, and compression rates of 0.43 %, 8.45 %, and 12.64 %, respectively. In real applications, the locking stress exceeds 2000 N. The second stuffing remains unaffected by deformation, with a maximum deformation of 6.3192×10^{-3} mm and a compression rate of 0.42 %. It serves as an insurance layer. The inner wall of the nut should be chamfered or polished to preserve the cable outer skin.
- With rising temperature, both the coefficient of thermal expansion and the thermal conductivity increase. The modulus of elasticity follows the opposite trend. The temperature at the weld was predominantly expressed by heat conduction and had a concentric circle distribution. The maximum temperatures at the weld are 362.05 °C, 451.72 °C, and 541.06 °C, with temperature loads of 35.629, 48.104, and 61.834 MPa, respectively, representing an increase of approximately 35.1 % and 28.5%. According to Fourier's rule of heat conduction, the larger the along-travel heat loss of heat, the boundary 50 mm from the weld experiences large thermal stresses, whereas the boundary 100 mm from the weld is mostly unaffected. With increased heating duration, the weld will still create thermal stress concentration. Therefore, in order to reduce the influence of thermal stress on the weld seal, the heater should be properly adjusted to avoid extended running of the heater at rated power during application. In addition, when the heater seems to run at rated power for a long period when the experiment necessitates it, the flow rate of the injected gas should be raised.
- The heater seal structure was optimized based on the numerical simulation results presented above. When the heater turns on, the temperature of the heating rod and outlet quickly rises to 400 ℃. At the start of heat injection, the injected gas flow rate is low, and the gas cannot entirely remove the heat created by the heating rod; nevertheless, as the injected flow rate gradually increases, both of them exhibit the opposite trend of change. The exit temperature is maintained at 400 ℃, while the heating rod is kept between 210 ℃ and 220 ℃. Increasing the power of the heating rod leads to a steady increase in both the outlet temperature and the heating rod directly. For every 100 ℃ increase in the outlet temperature, the surface temperature of the heating rod rises by 20-25 ℃. The heating rod heat accumulation will heat both the heater and the gas in the injection well, preheating the injection gas ahead of time. This test demonstrates that this type of sealing procedure can produce good sealing results. Maintain the stability of good sealing.

ACKNOWLEDGEMENTS

This research was funded by the National Key R&D Program of China (Grant No., Grant No.2019YFA0705501), the Young and Middle-aged Excellent Team Project for Scientific and Technological Innovation of Jilin Province of China (Grant No.20220508135RC), the Independent Innovation Capacity Project of Jilin Province Development and Reform Commission (Grant No.2022C021) the Program for JLU Science and Technology Innovative Research Team (Grant No.2020TD-05), Science and technology research project of Education Department of Jilin Province（JJKH20231185KJ） and the Fundamental Research Funds for the Central Universities.

REFERENCES

[1] P. C. Slorach and L. Stamford, "Net zero in the heating sector: Technological options and environmental sustainability from now to 2050," *Energy Convers. Manage.*, vol. 230, no. 3, p. 113838, Feb 2021, doi: 10.1016/j.enconman.2021.113838.

[2] W. He, Y. Sun, and X. Shan, "Organic matter evolution in pyrolysis experiments of oil shale under high pressure: Guidance for in situ conversion of oil shale in the Songliao basin," *J. Anal. Appl. Pyrolysis*, vol. 155, no. 6, p. 105091, May 2021, doi: 10.1016/j.jaap.2021.105091.

[3] X. Pang *et al.*, "Main controlling factors and movability evaluation of continental shale oil," *Earth-Sci. Rev.*, vol. 243, p. 104472, Aug 2023, doi: 10.1016/j.earscirev.2023.104472.

[4] Y. Gao, T. Wan, Y. Dong, and Y. Li, "Numerical and experimental investigation of production performance of in-situ conversion of shale oil by air injection," *Energy Reports*, vol. 8, no. 8, pp. 15740-15753, Nov 2022, doi: 10.1016/j.egyr.2023.01.119.

[5] W. Guo, Q. Li, S. Deng, Y. Wang, and C. Zhu, "Mechanism and reservoir simulation study of the autothermic pyrolysis in-situ conversion process for oil shale recovery," *Pet. Sci.*, vol. 20, no. 2, pp. 1053-1067, 2023, doi: 10.1016/j.petsci.2022.08.030.

[6] Z. Wang *et al.*, "Economic and heating efficiency analysis of double-shell downhole electric heater for tar-rich coal in-situ conversion," *Case Studies in Thermal Engineering*, vol. 41, p. 102596, Jan 2023, doi: 10.1016/j.csite.2022.102596.

[7] H. Liu, T. Sun, Y. Zhang, B. Wu, Z. Wang, and Y. Fan, "Design of oil shale in-situ extraction heater structure and numerical simulation of the fracturing process," *Chem. Technol. Fuels Oils*, vol. 58, no. 6, pp. 990-1004, Jan 2023, doi: 10.1007/s10553-023-01481-0.

[8] M. J. B. Montilla, S. Li, Z. Zhang, X. Li, Y. Sun, and S. Ma, "Theoretical analysis of the effect of electrical heat in situ injection on the kerogen decomposition for the development of shale oil deposits," *Energies*, vol. 16, no. 13, p. 5007, Jul 2023, doi: 10.3390/en16135007.

[9] H. Shui, Y. Wang, Z. Liu, and W. Guo, "Optimal parameter adjustment of catalytic combustion heaters for oil shale in-situ conversion of low calorific value gases," *J. Cleaner Prod.*, vol. 426, Nov 2023, doi: 10.1016/j.jclepro.2023.139020.

[10] T. Sun, H. Liu, T. Yan, and Y. Zhang, "Numerical study on enhanced heat transfer of downhole slottedtype heaters for in situ oil shale exploitation," *Acs Omega*, vol. 8, no. 39, pp. 36043-36052, Sep 2023, doi: 10.1021/acsomega.3c04099.

[11] A. H. Altun and O. Ziylan, "Experimental investigation of the effects of horizontally oriented vertical sinusoidal wavy fins on heat transfer performance in case of natural convection," *Int. J. Heat Mass Transfer*, vol. 139, pp. 425-431, 2019.

[12] Y. Chen, H. Zeng, J. Wang, H. Chen, and J. Zhu, "Heat transfer performance of a downhole electric tubular resistive heater.," *Appl. Sci.*, vol. 12, no. 19, p. 9508, Oct 2022, doi: 10.3390/app12199508.

[13] X. Li and Y. Yang, "Experimental study of sealing performance test methods and sealing mechanism of shield tail sealing grease," *J. Test. Eval.*, vol. 49, no. 5, pp. 3366-3377, Sep 2021, doi: 10.1520/jte20190833.

[14] X. Liang, D. Hu, Y. Li, Y. Zhang, and X. Yang, "Application of GPR underground pipeline detection technology in urban complex geological environments," *Geofluids*, vol. 2022, no. 1, p. 7465919, May 2022, doi: 10.1155/2022/7465919.

[15] I. Amanzhol, N. Zholmagambetov, D. Abitaev, S. Kusherbayev, and A. Mereke, "Assessment and analysis of occupational risks in underground mining of polymetallic ores," *International Journal of Geomate*, vol. 25, no. 109, pp. 101-108, Sep 2023, doi: 10.21660/2023.109.m2309.

[16] H. Brakelmann, G. J. Anders, and P. Zajac, "Fundamentals of the thermal analysis of complex arrangements of underground heat sources," *Energies*, vol. 14, no. 20, p. 6813, Oct 2021, doi: 10.3390/en14206813.

[17] G. Hu, G. Wang, L. Dai, P. Zhang, M. Li, and Y. Fu, "Sealing failure analysis on v-shaped sealing rings of an inserted sealing tool used for multistage fracturing processes," *Energies*, vol. 11, no. 6, p. 1432, Jun 2018, doi: 10.3390/en11061432.

[18] S. Wang, P. Liu, D. Li, Z. Dong, and G. Li, "Simulation and experimental study on sealing characteristics of hydro-pneumatic spring GS seal rings," *Appl. Sci.*, vol. 13, no. 21, p. 11703, Nov 2023, doi: 10.3390/app132111703.

[19] Y. Hu, J. Zhang, and L. Chen, "Design and seal performance analysis of bionic sealing ring for dynamic seal," *Mechanika*, vol. 26, no. 4, pp. 338-345, 2020, doi: 10.5755/j01.mech.26.4.23264.

[20] Y. Takigahira, Y. Maetani, M. Ito, N. Uemura, and K. Ohashi, "Study on additively manufactured mechanical seal (part 1) -numerical analysis and experimental study on static characteristics," *Tribology Online*, vol. 17, no. 4, pp. 306-317, 2022, doi: 10.2474/trol.17.306.

[21] Q. Zhang, Q. Wang, X. Tan, and J. Zhang, "Unsteady numerical investigation on the sealing effectiveness and flow field in different rim seal geometries," *Aerospace*, vol. 9, no. 12, p. 780, Dec 2022, doi: 10.3390/aerospace9120780.

[22] F. F. Foko, C. Burkhart, S. Thielen, and B. Sauer, "Analysis of the sealing capability of radial shaft sealing rings using a semi-analytical contact model," *Tribology Online*, vol. 17, no. 2, pp. 97-109, 2022, doi: 10.2474/trol.17.97.

[23] Y. Liu, W. Li, and C. Xia, "Research on sealing mechanism and structural improvement of metal sealing structures for high speed drill bits," *Int. J. Pressure Vessels Piping*, vol. 207, p. 105104, Feb 2024, doi: 10.1016/j.ijpvp.2023.105104.

[24] B. Bamps, K. D'Huys, I. Schreib, B. Stephan, B. De Ketelaere, and R. Peeters, "Evaluation and optimization of seal behaviour through solid contamination of heat-sealed films," *Packag. Technol. Sci.*, vol. 32, no. 7, pp. 335-344, Jul 2019, doi: 10.1002/pts.2442.
[25] Z. Wang, Q. Liu, Y. Lou, H. Jin, and Z. Suo, "Elastic leak for a better seal," *Journal of Applied Mechanics-Transactions of the Asme*, vol. 82, no. 8, p. 081010, Aug 2015, doi: 10.1115/1.4030660.
[26] W. Xu *et al.*, "Evolution of organic carbon isotopes during the pyrolysis of Nongan oil shale in Songliao basin and its implications for in-situ conversion project," *Geomechanics and Geophysics for Geo-Energy and Geo-Resources*, vol. 9, no. 1, p. 65, Dec 2023, doi: 10.1007/s40948-023-00616-1.
[27] D. Cheng, L. Gu, Y. Sun, and Y. Shi, "Numerical calculation method of multi-lip seal wear under mixed thermal elastohydrodynamic lubrication," *Lubricants*, vol. 11, no. 6, p. 248, Jun 2023, doi: 10.3390/lubricants11060248.
[28] Z. Li, S. Li, X. Wang, and D. Li, "Numerical simulation and experimental study on magnetorheological fluid seals with flexible pole pieces," *IEEE Trans. Magn.*, Article vol. 57, no. 10, pp. 1-7, Oct 2021, doi: 10.1109/tmag.2021.3094868.
[29] G. Hou, H. Su, G. Chen, and Y. Tian, "Performance analysis of compliant cylindrical intershaft seal," *Science Progress*, vol. 103, no. 3, Jul 2020, doi: 10.1177/0036850420941957.
[30] Y. Zhao, H. Yan, S. Dong, T. Jiang, and H. Jiang, "Experimental research on the friction and leakage of the metal rubber seal for reciprocating motion," *Proceedings of the Institution of Mechanical Engineers Part J-Journal of Engineering Tribology*, vol. 236, no. 11, pp. 2221-2231, Nov 2022, doi: 10.1177/13506501221074784.
[31] X. Zhang, J. Jiang, X. Peng, and Z. Ni, "Experimental and numerical simulation study on the influence of structural factors on the leakage characteristics of clearance seals," *Flow Meas. Instrum.*, vol. 94, p. 102465, Dec 2023, doi: 10.1016/j.flowmeasinst.2023.102465.
[32] Y. Zhu *et al.*, "A case study on the optimal design of the horizontal wellbore trajectory for hydraulic fracturing in Nong'an oil shale," *Energies*, vol. 13, no. 1, p. 286, Jan 2020, doi: 10.3390/en13010286.
[33] C. Er *et al.*, "Relationship between tight reservoir diagenesis and hydrocarbon accumulation: An example from the early Cretaceous Fuyu reservoir in the Daqing oil field, Songliao basin, China," *J. Pet. Sci. Eng.*, vol. 208, p. 109422, Jan 2022, doi: 10.1016/j.petrol.2021.109422.
[34] S. Si *et al.*, "Oil charging power simulation and tight oil formation of Fuyu oil layer in Sanzhao area, Songliao basin," *Frontiers in Earth Science*, vol. 10, p. 825548, Apr 2022, doi: 10.3389/feart.2022.825548.
[35] B. Zhang, D. Kang, S. Ma, W. Duan, and Y. Zhang, "Densification and fracture type of desert in tight oil reservoirs: A case study of the Fuyu tight oil reservoir in the Sanzhao depression, Songliao basin," *Lithosphere*, vol. 2021, no. 4, p. 2609923, Jul 2021, doi: 10.2113/2021/2609923.
[36] K. I. Adeniyi, M. Zirrahi, and H. Hassanzadeh, "Phase equilibria of water-hydrocarbon (pentane to heavy oils) systems in the near-critical and supercritical water regions - A literature review," *J. Supercrit. Fluids*, vol. 178, p. 105356, Dec 2021, doi: 10.1016/j.supflu.2021.105356.
[37] Y. Sun, L. He, S. Kang, W. Guo, Q. Li, and S. Deng, "Pore evolution of oil shale during sub-critical water extraction," *Energies*, vol. 11, no. 4, p. 842, Apr 2018, doi: 10.3390/en11040842.
[38] A. A. Afanasyev, "On the numerical modeling of water flows in porous media under near-critical conditions," *Fluid Dyn.*, vol. 55, no. 8, pp. 1003-1011, Dec 2020, doi: 10.1134/s0015462820080029.
[39] Y. Yu, Y. Cui, H. Zhang, D. Wang, and J. Zhong, "Evaluation analysis on leakage performance for beam seal with two sealing areas," *IEEE Access*, vol. 10, pp. 29916-29924, 2022, doi: 10.1109/access.2022.3158485.
[40] R. G. Ferreira, A. P. Silva, and J. Nunes Pereira, "Current on-skin flexible sensors, materials, manufacturing approaches, and study trends for health monitoring: A review," *ACS Sens.*, vol. 9, no. 3, pp. 1104-1133, Feb 2024, doi: 10.1021/acssensors.3c02555.
[41] Y. Sun, Z. Liu, Q. Li, S. Deng, and W. Guo, "Controlling groundwater infiltration by gas flooding for oil shale in situ pyrolysis exploitation," *J. Pet. Sci. Eng.*, vol. 179, pp. 444-454, Aug 2019, doi: 10.1016/j.petrol.2019.04.055.
[42] Q. Bu, Q. Li, and X. Li, "Numerical heat transfer simulation of oil shale large-size downhole heater," *Appl. Sci.*, vol. 14, no. 6, p. 2235, Mar 2024, doi: 10.3390/app14062235.